Cyclic evolution of phytoplankton forced by changes in tropical seasonality

Luc L Beaufort, Clara Bolton, Anta-Clarisse Sarr, Baptiste Suchéras-Marx, Yair Rosenthal, Yannick Donnadieu, Nicolas Barbarin, Samantha Bova, Pauline Cornuault, Yves Gally, et al.

▶ To cite this version:

Luc L Beaufort, Clara Bolton, Anta-Clarisse Sarr, Baptiste Suchéras-Marx, Yair Rosenthal, et al.. Cyclic evolution of phytoplankton forced by changes in tropical seasonality. 2020. hal-03006397

HAL Id: hal-03006397
https://hal.science/hal-03006397

Preprint submitted on 19 Nov 2020

Cyclic evolution of phytoplankton forced by changes in tropical seasonality

Luc Beaufort[1*], Clara T. Bolton[1], Anta-Clarisse Sarr[1], Baptiste Suchéras-Marx[1], Yair Rosenthal[2], Yannick Donnadieu[1], Nicolas Barbarin[1§], Samantha Bova[2], Pauline Cornuault[1#], Yves Gally[1], Emmeline Gray[1&], Jean-Charles Mazur[1], Martin Tetard[1]

[1]Aix Marseille Univ, CNRS, IRD, INRAE, Coll France, CEREGE, Aix-en-Provence, France
[2]Rutgers University, Piscataway, USA
[§]Present address: TOTAL S.A., Pau, France
[#]Present address: Universität Bremen, MARUM, Bremen, Germany
[&]Present address: The Open University, Milton Keynes, UK
* To whom correspondence should be addressed: beaufort@cerege.fr

The effect of global climate cycles driven by Earth's orbital variations on evolution is poorly understood because of difficulties achieving sufficiently-resolved records of past evolution. The fossil remains of coccolithophores, a key calcifying phytoplankton group, enable an exceptional assessment of the impact of cyclic orbital-scale climate change on evolution because of their abundance in marine sediments, and because coccolithophores demonstrate extreme morphological plasticity in response to the changing environment[1,2]. Recently, evolutionary genetic analyses linked broad changes in Pleistocene fossil coccolith morphology to species radiation events[3]. Here, using high-resolution coccolith data, we show that during the last 2.8 million years coccolithophore evolution was forced by Earth's orbital eccentricity with rhythms of ~100,000 years and 405,000 years - a distinct spectral signature to that of coeval global climate cycles[4]. Simulations with an Earth System Model[5] including the marine carbon cycle[6] demonstrate that eccentricity directly impacts the diversity of ecological niches occurring over the annual cycle in the tropical ocean. Reduced seasonality favours species with mid-size coccoliths that bloom year-round, increasing coccolith carbonate export and burial. We posit that eccentricity pacing of phytoplankton evolution contributed to the strong 405,000-year pacing seen in records of the global carbon cycle.

Coccolithophores are important producers of $CaCO_3$ in the ocean and their fossil remains (calcite platelets called coccoliths) first appeared in sediments during the late Triassic (~210 million years ago, Ma). Coccolithophores rose to dominance in the open ocean during the early Cretaceous[7] and thereafter become a key biological modulator of the global carbon cycle, via both photosynthesis and calcification[8]. In the dominant Noëlaerhabdaceae family (including the cosmopolitan genera *Emiliania*, *Gephyrocapsa* and *Reticulofenestra*), species are defined by the morphological characteristics of their coccoliths, with size being a key criterion[9]. For *Gephyrocapsa* and *Emiliania*, phylogenies reconstructed from gene sequence data indicate that morphology-based definitions correspond to biological species[3,10]. Yet, within a given Noëlaerhabdaceae population, interspecific and intraspecific changes in coccolith length and mass (the latter encoding degree of calcification as well as size) occur in response to environmental parameters such as carbonate chemistry[1] and temperature[2]. Existing studies of coccolithophore evolution have focused on geological-timescale changes in species richness and turnover[11], coccolith carbonate accumulation[7,12], or calcification potentially driven by carbon cycle changes[13]. However, to date a lack of records that are both long-term and high-resolution has precluded an understanding of the impact of orbital cycles (on timescales of tens to hundreds of thousands of years) on coccolithophore evolution and carbonate production.

Here, we quantify the history of tropical Noëlaerhabdaceae evolution throughout the Pleistocene at high resolution (~2 thousand years, kyr), using coccoliths preserved in nine well-dated sedimentary sections from the tropical Indian and Pacific Oceans (Fig. 1; Extended Data Table 1; Methods). We use artificial intelligence microscopy to create an unprecedented biometric database of over 7 million coccoliths from >8000 samples (see Methods). The remarkable similarity of morphometric patterns observed at each site has led us to build evolutionary histograms of coccolith size and mass. To create these, we binned data into 30-kyr intervals to erase any precession-band variability driven by ecology[14] and to increase the statistical robustness of each point, now composed of measurements of tens of thousands of individual coccoliths (Fig. 2a; Methods). Evolutionary histograms for size and mass show identical trends and variability, we therefore only discuss the size record. The data show multiple phases of contraction alternating with phases of dilation characterised by bimodal or broader morphological distributions (Fig. 2a). Patches of high abundance of a particular morphotype correspond in many cases to described acmes of Noëlaerhabdaceae species[15-17]. The most recent dilation phase that started around 450 thousand years ago (ka) has been attributed to a radiation event and the emergence of new *Gephyrocapsa* species, based on a consensus phylogeny reconstructed from genome sequence data and its temporal correlation to low-resolution coccolith morphometric data[3]. Over the entire record, average coccolith size shows an increasing trend that corresponds to a gradual shift in dominance from smaller to larger coccoliths during the Pleistocene (Fig. 2b). On orbital time scales, coccolith size and global ice volume and temperature cycles as represented by the $\delta^{18}O$ of benthic foraminifers[18] show very different temporal evolution (Fig. 2c). Instead the size contraction and dilation alternations follow a regular cycle that is highly coherent (>99.9%) with the orbital eccentricity periods of 405 kyr (e405) and of 124 and 95 (e100)[19] (Extended Data Figure 1a), with contractions (dilations) occurring at low (high) eccentricity with a slight time lag (Fig. 2b).

The average size or mass of coccoliths in a Noëlaerhabdaceae population may vary over time because of macro- and/or micro-evolution, or because ecological changes modulate the relative abundances of species in different size ranges. To remove the effect of relative abundance changes, we create a novel Morphological Divergence Index, MDI, that represents the difference in average coccolith mass between two size classes, larger and smaller than 3μm (Extended Data Figure 2; Methods). MDI records from individual sites are highly intercorrelated (Extended Data Figure 3) and all show significant e405 and e100 periods (Extended Data Figure 1), despite coming from distinct oceanographic biomes[20] and climatic regimes (e.g. Warm Pool, monsoon-dominated; see Extended Data Table 1). We therefore produce a composite MDI stack, preserving the high resolution of each dataset (Fig. 3c; Methods). Evolutionary cross-spectral analysis indicates that the stack has highly significant (>90%) coherency with the frequencies of Earth's eccentricity since 2.8 Ma (Fig. 3b, b'). This pattern cannot be the result of differential dissolution on coccolith morphology, because MDI values are similar regardless of core depths, and because in contrast to MDI, Pleistocene deep-sea $CaCO_3$ dissolution generally follows a glacial-interglacial (G-IG) pattern[21]. The MDI stack, interpreted as primarily reflecting evolutionary changes in morphology, shows strong 405-kyr pacing throughout the Pleistocene, irrespective of G-IG background state. While eccentricity forcing on coccolithophore productivity has previously been suggested[22,23], our new high-resolution multi-million-year dataset reveals that eccentricity cycles imprinted the evolution of the Noëlaerhabdaceae. Such cyclicity may have had important consequences for the oceanic carbon cycle on multiple time scales via coccolith carbonate production and burial in sediments[12,24]. Coccolithophores are known to produce high amounts of calcite during blooms[22,25], and sediments are often dominated by few species, for example *Emiliania huxleyi* (0-90 ka)[15] and *Gephyrocapsa caribbeanica* (280-570 ka)[16] in the late Pleistocene. We estimate the $CaCO_3$ mass accumulation rate (MAR) of Noëlaerhabdaceae coccoliths in our cores and produce a stacked $CaCO_3$ MAR record (Fig. 3e, Methods). This reveals that higher MARs correspond to lower MDI values when mid-size bloom species, which contribute the most to coccolith carbonate export, dominate. The dominance of these bloom species coupled with high coccolithophore production and accumulation in sediments during eccentricity minima is also recorded in the extra-tropics[22], attesting to the global significance of these observations. In our records, the two main components, production of coccoliths and individual mass, often have opposing effects on MAR since medium-size and low-mass species, such as *E. huxleyi* and *G. carribeanica*, are the most productive (Extended Data Figure 4). In addition, local ecological conditions affecting productivity and export, and potentially water depth affecting coccolith preservation, likely also influence MAR, although it is not possible to quantify the relative effects of these factors. Nevertheless, the composite MAR record shows strong eccentricity periodicities that are significantly coherent with MDI throughout the Pleistocene (Fig. 3d, d'), demonstrating a strong imprint of coccolithophore evolution on carbonate production and burial.

MDI as a recorder of seasonality

We hypothesise that our new coccolith index reflects variations in the amplitude of tropical seasonality. In low latitudes, seasonal contrast is related to the eccentricity of Earth's orbit, (1) directly because the ellipticity of the orbit determines the distance between the Sun and the Earth during each season, affecting radiation intensity, and (2) indirectly because eccentricity modulates the effect of precession on seasonal insolation contrast. Seasonal contrast is greater during periods of high eccentricity. To our knowledge, the eccentricity-paced rhythm of surface-ocean seasonality that dominates MDI has not been documented previously because most proxies record integrated annual average conditions or a specific season. The seasonal succession of coccolithophore species, a characteristic of phytoplankton ecology, is indicative of their adaptation to the different ecological niches created by seasons[26]. Those seasonal niches are more diverse in a climate with stronger seasonality[20]. In the modern ocean, the highest phytoplankton diversity is found in the tropical band, a pattern probably related to high temperatures and temporal stability, whereas the seasonal species turnover is highest at mid-latitudes because of a strong seasonal contrast[27]. Annual records of Net Primary Production (NPP) are good descriptors of the range of oceanographic niches and biomes[20]. To demonstrate the effect of orbital configuration on NPP and therefore niche availability, we simulated monthly oceanic NPP using the fully-coupled IPSL-CM5A-2 model[6], which includes the ocean biogeochemistry model PISCES-v2[5], for seven early Pleistocene time intervals chosen to cover a large eccentricity spectrum with different precession conditions but with similar ice volume and obliquity (lines in Fig. 2; Extended Data Table 2). The results of these simulations for the tropical eastern Indian and western Pacific Oceans show that the seasonal range of NPP increases with eccentricity, a trend that parallels the eccentricity sorted values of MDI (Fig. 4).

In the simulations, the increase in the amplitude of the NPP seasonal cycle (Fig 1; Extended Data Figure 5b-e) is primarily driven by higher productivity during boreal summer, especially in the eastern Indian ocean. This increase is forced by modification of atmosphere-ocean dynamics in response to variations in the amplitude and seasonality of insolation forcing that is amplified at extreme eccentricity values (Extended Data Figure 5g-j and 6a-c). During high eccentricity periods at precession minima (maxima), increasing (decreasing) boreal summer insolation (Extended Data Figure 6b, c) is responsible for increasing (decreasing) sea-level pressure over continental Asia (Extended Data Figure 6e-h). Induced modifications of sea-level pressure gradients over the tropical Indian and Pacific Oceans in turn translate into changes in the low-level wind circulation over the Indo-Pacific Warm Pool, IPWP, (Extended Data Figure 5g-j). Anomalous easterlies at precession minima (westerlies at precession maxima) in the equatorial region generate anomalous upwelling along the equator (SW of India) that are responsible for the increasing nutrient content at the surface triggering large enhancement of productivity (Extended Data Figure 7a-c). NPP is, in addition, amplified by modifications of the hydrological cycle that create more favourable conditions related to changes in salinity, water temperature and/or amount of solar radiation at the surface. At maximum precession and eccentricity, for example, higher sub-surface salinity (+0.5 to 1.6 psu) and lower temperatures (-1.2 to -2°C) in the western Bay of Bengal relative to in other simulations (Extended Data Figure 7c) reduce stratification of the upper-water column, which favours vertical mixing and contributes to enhanced productivity. Overall, those localized increases in the amplitude of the seasonal cycle lead to a less homogeneous upper ocean in the IPWP region at high eccentricity (Fig. 1 and Extended Data Figure 5a-c). We propose that during high eccentricity times, the higher seasonal range of NPP in our model simulations is indicative of more diverse ecological niches that coccolithophores can adapt to. A greater diversity of ecological niches when seasonality is high[20] leads to a larger range of morphotypes because Noëlaerhabdaceae adaptation is characterised by the adjustment of coccolith size and degree of calcification (therefore mass) to thrive in the new environments[1,2].

Eccentricity lags, species origination, and dominance

The MDI reflects periods of dominance of a particular species or morphotype, rather than species origination events, and is clearly modulated by eccentricity. In stark contrast to most Pleistocene climate proxy records (e.g.[14,18]), precession and obliquity cycles are absent from the high-resolution MDI records (Extended Data Figure 3), suggesting that evolutionary processes smooth the records. Significant lags exist between eccentricity forcing and coccolith morphology (Fig. 2b), which we hypothesize result from the time taken for favourable conditions to reoccur that allow a species to rise to dominance following its first emergence. For example, *E. huxleyi* first appeared at 290 ka, but did not become dominant until 90 ka[15]. Yet speciation events spread rapidly throughout the oceans[15,17], a phenomenon reflected in the small genetic diversity amongst the global Noëlaerhabdaceae population[10]. This time lag could result from interspecific competition. When *E. huxleyi* originated, *Gephyrocapsa oceanica* and *Gephyrocapsa ericsonii* already dominated coccolithophore assemblages, and the time required for *E. huxleyi* to become widespread while favourable conditions persisted was not sufficient for it to become dominant. It was not until two e100 cycles later, under similar eccentricity conditions, that *E. huxleyi* gained a competitive advantage and rose to dominance. The delay between species appearance and dominance is thus intrinsic in the MDI record, acting as a low pass-filter with a cut-off frequency of 1/200 kyr-1 (Fig. 2b, Extended Data Figure 8). For other species, the lag might have been one or two e100 cycle, providing an explanation for the non-stationary nature of the phase lag between e100 and MDI.

Long-eccentricity forcing, coccolithophores, and the global carbon cycle

The persistence of the long eccentricity cycle e405 in Cenozoic and Mesozoic records of the ocean carbon cycle (e.g., weight percent $CaCO_3$ and foraminiferal $\delta^{13}C$)[28-30], independent of G-IG climate state, testifies to the importance of biogeochemical processes operating at this timescale throughout Earth's history. In the Pleistocene, Mediterranean surface $\delta^{13}C$ records record e405 cycles more faithfully than deep open-ocean sites, suggesting a low-latitude climatic origin of this signal[23]. Similar to our coccolith records, a significant phase lag between $\delta^{13}C$ and eccentricity is observed in the e405 band, which has been explained by the long residence time of carbon in the oceans and resultant transfer of energy from precession into eccentricity bands via a non-linear process[28]. Previous studies spanning up to ~1 Myr have linked coccolithophore production to eccentricity forcing[14,22]. However, the hypothesis proposed by Rickaby *et al.*[22] that eccentricity-driven changes in growing season length may be responsible for the ~400-kyr cycle in coccolithophore production cannot adequately explain changes reconstructed at our low latitude sites. Instead, our data and model results lead us to the alternative hypothesis that changes in seasonality caused by the eccentricity of the Earth's orbit paced tropical Noëlaerhabdaceae production and evolution throughout the Pleistocene. Although these changes clearly impact carbonate accumulation patterns (Fig. 3), coccolithophore productivity alone cannot be responsible for the expression of long eccentricity cycles in climate records. Other phytoplankton groups, some with little or no fossil record, must also have been influenced by variations in tropical seasonality on these timescales. In this case, the impact of changes in the ratio of exported organic carbon production to carbonate mineral production, known as the rain ratio[31], may have been strong enough to modulate the carbon cycle. Our data, showing cyclic evolution of calcifying phytoplankton on eccentricity timescales in response to seasonality, provide a new perspective in support of the hypothesis of Pälike *et al.*[28] that biosphere productivity must have responded directly to changes in solar insolation in order to explain the strong e405 signature in carbon cycle records.

Main references

1 Beaufort, L. *et al.* Sensitivity of coccolithophores to carbonate chemistry and ocean acidification. *Nature* **476**, 80-84, doi: 10.1038/nature10295 (2011).

2 Henderiks, J. & Bollmann, J. The *Gephyrocapsa* sea surface palaeothermometer put to the test: comparison with alkenone and foraminifera proxies off NW Africa. *Mar. Micropaleontol.* **50**, 161-184, doi: 10.1016/S0377-8398(03)00070-7 (2004).

3 Bendif, E. M. *et al.* Repeated species radiations in the recent evolution of the key marine phytoplankton lineage *Gephyrocapsa*. *Nat. Commun.* **10**, 4234, doi:10.1038/s41467-019-12169-7 (2019).

4 Ruddiman, W. F. & Raymo, M. E. in *The past three million years : Evolution of climatic variability in the North Atlantic Region* (eds N.J. Shackleton, R.G. West, & D.Q Bowen) (University Press, 1988).

5 Sepulchre, P. *et al.* IPSL-CM5A2 – an Earth system model designed for multi-millennial climate simulations. *Geosci. Model Dev.* **13**, 3011-3053, doi:10.5194/gmd-13-3011-2020 (2020).

6 Aumont, O., Éthé, C., Tagliabue, A., Bopp, L. & Gehlen, M. PISCES-v2: An ocean biogeochemical model for carbon and ecosystem studies. *Geosci. Model Dev.* **8**, 2465-2513, doi: 10.5194/gmd-8-2465-2015 (2015).

7 Suchéras-Marx, B. *et al.* The colonization of the oceans by calcifying pelagic algae. *Biogeosciences* **16**, 2501-2510, doi: 10.5194/bg-16-2501-2019 (2019).

8 Ridgwell, A. & Zeebe, R. E. The role of the global carbonate cycle in the regulation and evolution of the Earth system. *Earth Planet. Sc. Lett.* **234**, 299-315, doi: 10.1016/j.epsl.2005.03.006 (2005).

9 Perch-Nielsen, K. in *Plankton Stratigraphy* Vol. 1 (eds H.M. Bolli, J.B. Saunders, & K. Perch-Nielsen) Ch. Cenozoic calcareous nannofossils, 427-458 (Cambridge University Press, 1985).

10 Filatov, D. A. Extreme Lewontin's paradox in ubiquitous marine phytoplankton species. *Mol. Biol. Evol.* **36**, 4-14, doi:10.1093/molbev/msy195 (2019).

11 Bown, P. R. Calcareous nannoplankton evolution: a tale of two oceans. *Micropaleontol.* **51**, 299-308, doi: 10.2113/gsmicropal.51.4.299 (2005).

12 Si, W. & Rosenthal, Y. Reduced continental weathering and marine calcification linked to late Neogene decline in atmospheric CO_2. *Nat. Geosci.* **12**, 833-838, doi:10.1038/s41561-019-0450-3 (2019).

13 Bolton, C. T. *et al.* Decrease in coccolithophore calcification and CO_2 since the middle Miocene. *Nat. Commun.* **7**, 1-13 (2016).

14 Beaufort, L. *et al.* Insolation cycles as a major control of equatorial Indian ocean primary production. *Science* **278**, 1451-1454, doi: 10.1126/science.278.5342.1451 (1997).

15 Thierstein, H. R., Geitzenauer, K. R., Molfino B. & Shackleton, N. J. Global synchroneity of late Quaternary coccolith datum levels: validation by oxygen isotopes. *Geology* **5**, 400-404, doi: 10.1130/0091-7613(1977)5<400:GSOLQC>2.0.CO;2 (1977).

16 Bollmann, J., Baumann, K. H. & Thierstein, H. R. Global dominance of *Gephyrocapsa* coccoliths in the Late Pleistocene: Selective dissolution, evolution, or global environmental change? *Paleoceanography* **13**, 517-529, doi:10.1029/98PA00610 (1998).

17 Raffi, I. *et al.* A review of calcareous nannofossil astrobiochronology encompassing the past 25 million years. *Quaternary Sci. Rev.* **25**, 3113-3137, doi:https://doi.org/10.1016/j.quascirev.2006.07.007 (2006).

18 Lisiecki, L. E. & Raymo, M. E. A Pliocene-Pleistocene stack of 57 globally distributed benthic $\delta^{18}O$ records. *Paleoceanography* **20**, doi:10.1029/2004PA001071 (2005).

19 Laskar, J. *et al.* A long-term numerical solution for the insolation quantities of the Earth. *Astron. Astrophys.* **428**, 261-285, doi:10.1051/0004-6361:20041335 (2004).

20 Longhurst, A. *Ecological Geography of the Sea*. Vol. 1 (Academic Press, 1998).

21 Sexton, P. F. & Barker, S. Onset of 'Pacific-style' deep-sea sedimentary carbonate cycles at the mid-Pleistocene transition. *Earth Planet. Sc. Lett.* **321-322**, 81-94, doi:https://doi.org/10.1016/j.epsl.2011.12.043 (2012).

22 Rickaby, R. E. M. *et al.* Coccolith chemistry reveals secular variations in the global ocean carbon cycle? *Earth Planet. Sc. Lett.* **253**, 83-95, 10.1016/j.epsl.2006.10.016 (2007).

23 Wang, P., Tian, J. & Lourens, L. J. Obscuring of long eccentricity cyclicity in Pleistocene oceanic carbon isotope records. *Earth Planet. Sc. Lett.* **290**, 319-330, doi:https://doi.org/10.1016/j.epsl.2009.12.028 (2010).

24 Suchéras-Marx, B. & Henderiks, J. Downsizing the pelagic carbonate factory: Impacts of calcareous nannoplankton evolution on carbonate burial over the past 17 million years. *Global Planet. Change* **123**, 97-109, doi: 10.1016/j.gloplacha.2014.10.015 (2014).

25 Holligan, P. M. *et al.* A biogeochemical study of the coccolithophore, *Emiliania huxleyi*, in the North Atlantic. *Global Biogeochem. Cy.* **7**, 879-900, doi: 10.1029/93GB01731 (1993).

26 Okada, H. & McIntyre, A. Seasonal distribution of modern Coccolithophores in the western North Atlantic Ocean. *Mar. Biol.* **54**, 319-328, doi: 10.1007/BF00395438 (1979).

27 Righetti, D., Vogt, M., Gruber, N., Psomas, A. & Zimmermann, N. E. Global pattern of phytoplankton diversity driven by temperature and environmental variability. *Sci. Adv.* **5**, eaau6253, doi:10.1126/sciadv.aau6253 (2019).

28 Pälike, H. *et al.* The Heartbeat of the Oligocene Climate System. *Science* **314**, 1894-1898, doi:10.1126/science.1133822 (2006).

29 Herbert, T. D. A long marine history of carbon cycle modulation by orbital-climatic changes. *P. Natl Acad. Sci. USA* **94**, 8362-8369, doi: 10.1073/pnas.94.16.8362 (1997).

30 Kocken, I. J., Cramwinckel, M. J., Zeebe, R., Middelburg, J. & Sluijs, A. The 405 kyr and 2.4 Myr eccentricity components in Cenozoic carbon isotope records. *Clim. Past* **15**, 91-104, doi: 10.5194/cp-15-91-2019 (2019).

31 Archer, D. & Maier-Reimer, E. Effect of deep-sea sedimentary calcite preservation on atmospheric CO_2 concentration. *Nature* **367**, 260-263, doi: 10.1038/367260a0 (1994).

Figures

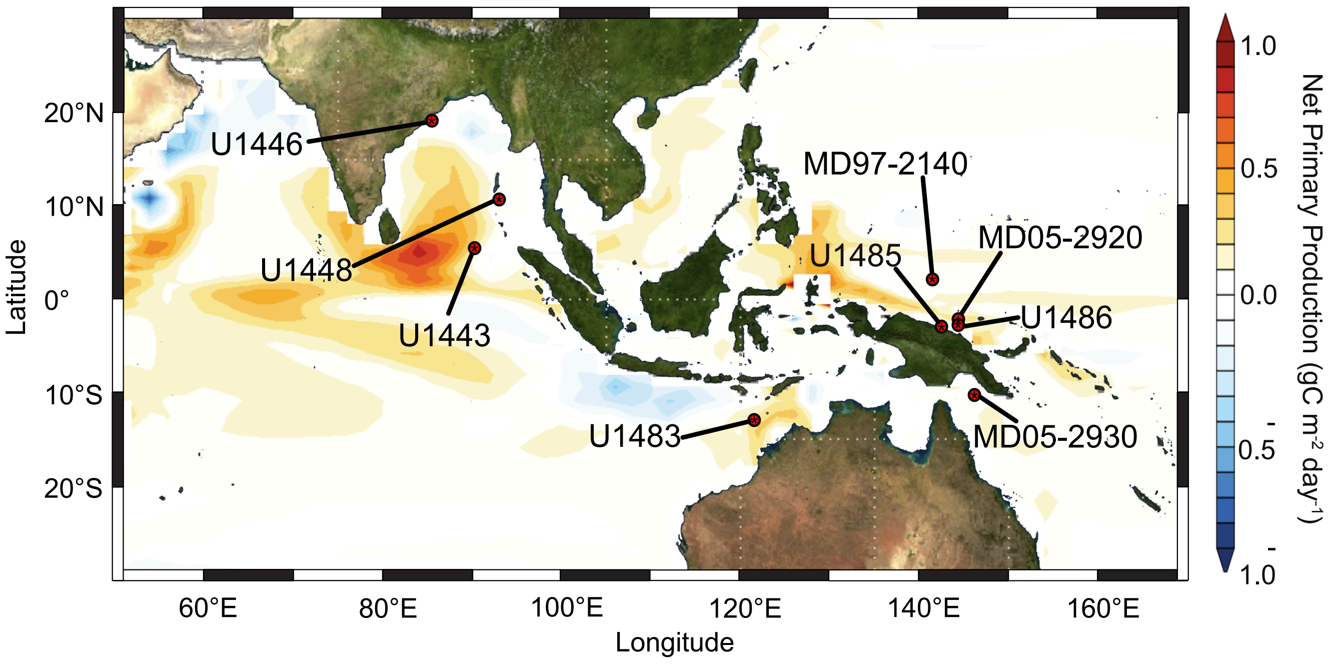

Figure 1: Core site locations and eccentricity-driven changes in seasonality of primary production in the tropical Indo-Pacific. Colour scale shows the vertically integrated net primary productivity difference between numerical model outputs computed at maximum and minimum eccentricity, each run at perihelion in June (Pmin) and December (Pmax) and then averaged (see Methods). Red (blue) colours imply higher (lower) seasonality at high eccentricity compared to low eccentricity.

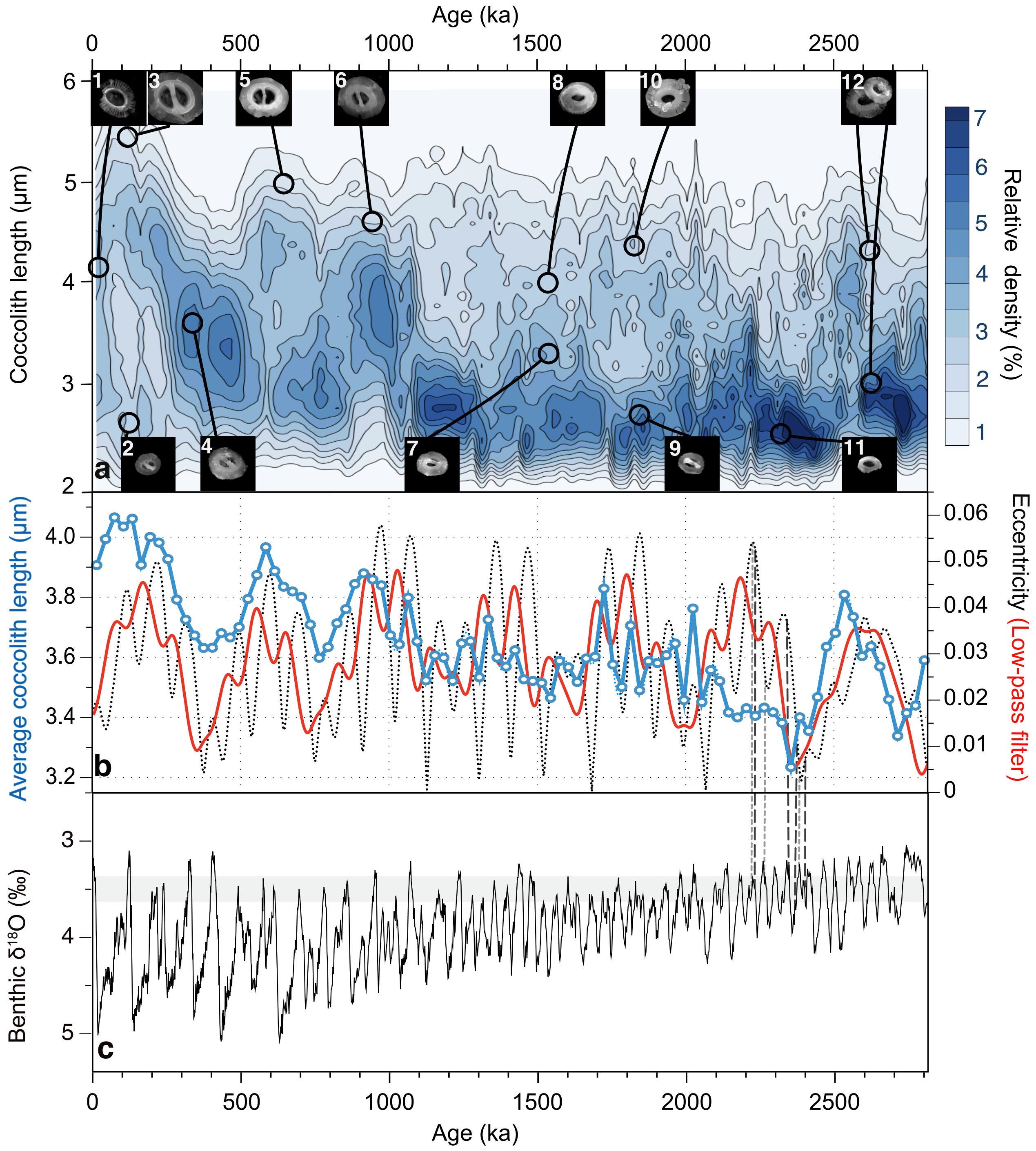

Figure 2: Coccolith size variability over the last 2.8 million years. a: Evolutionary histogram of coccolith length. Samples in each core were grouped into 30 kyr bins, standardised (%) and merged into a single stack (see Methods). Length bins are 0.1 μm. Scanning electron microscope images represent typical Noëlaerhabdaceae morphologies. 1: *Emiliania huxleyi*, 2: *Gephyrocapsa ericsonii*, 3: *Gephyrocapsa oceanica*, 4: *Gephyrocapsa caribbeanica*, 5-6: *Gephyrocapsa omega*, 7-8: mid-size *Gephyrocapsa*, 9: small *Gephyrocapsa*, 10: *Pseudoemiliania ovata*, 11: *Reticulofenestra minuta*, 12: left: *P. ovata*, right: *Reticulofenestra minutula*. **b**: Average length (blue) of coccoliths in the multi-site stack, plotted with Earth's eccentricity[19] (dotted black line) and low-pass filtered eccentricity with an angular frequency of 0.021 kyr^{-1} (red) and average coccolith length detrended (blue). **c**: LR04 benthic foraminiferal δ^{18}O stack[18]. Vertical dashed lines between panels b and c show orbital configurations used in model simulations (black long dash = Pmin, grey short dash = Pmax; see Methods). Grey band in c illustrates the small range of benthic δ^{18}O between simulations.

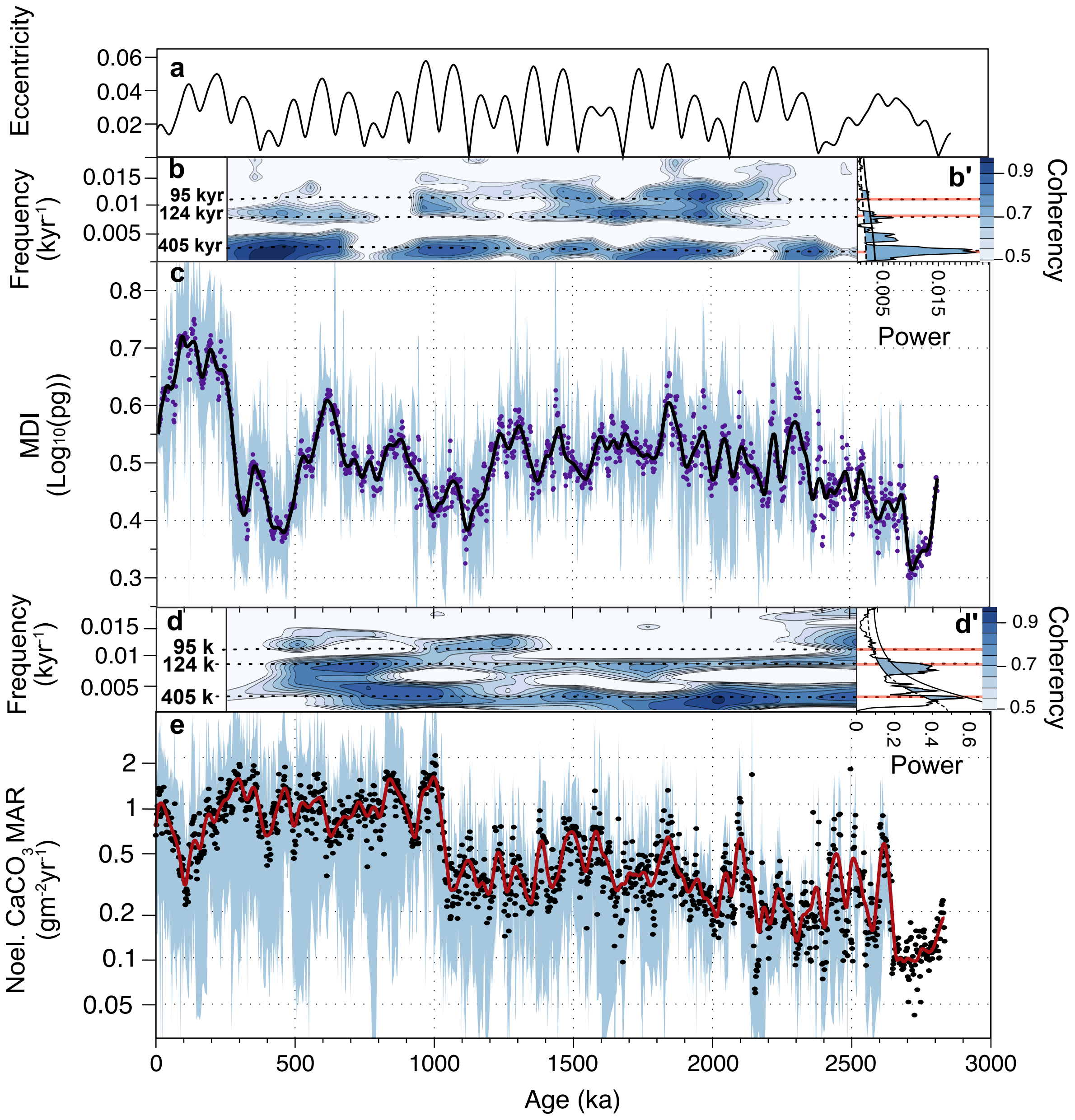

Figure 3: **Eccentricity, coccolith morphological divergence, and Noëlaerhabdaceae $CaCO_3$ mass accumulation rates**. **a**: Earth's eccentricity[19], **b**: Evolutive cross-spectral analysis between MDI and eccentricity (see Methods). Colour-scale shows coherency (90% Confidence Level (CL) above 0.7); Horizontal dashed lines show eccentricity periods. **b'**: MTM spectral analysis of detrended MDI stack. Shaded areas are above the 90%CL (dashed line). Solid black line is 95%CL. Frequency scale is aligned with b. **c**: MDI Stack (2 kyr resolution, see Methods). Blue shading shows maximum and minimum values from all records. **d**: Evolutive cross-spectral analysis between MAR and MDI (CLs as in b). **d'**: MTM spectral analysis of detrended MAR stack. CLs as in b'. **e**: Noëlaerhabdaceae $CaCO_3$ MAR stack (2 kyr resolution, see Methods). Blue shading shows maximum and minimum values from all records. MDI and MAR stacks are smoothed with a LOESS function.

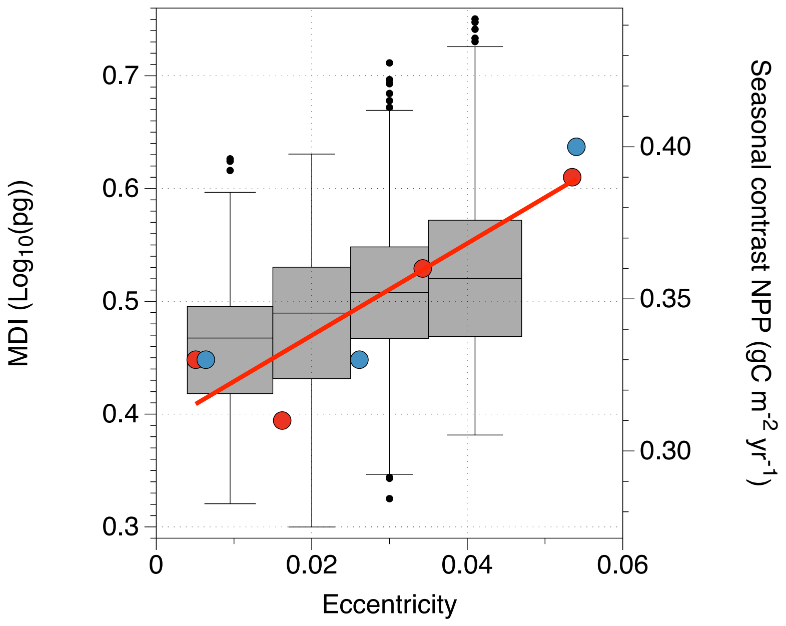

Figure 4: Morphological divergence index and modelled seasonality both increase with eccentricity. Box-whiskers plot of all MDI values, sorted and binned by increasing low-pass filtered eccentricity, compared to the seasonal contrast of net primary production (maximum minus minimum month) from numerical simulations (see Methods). Blue dots are model runs with perihelion in December (Pmax: 2222 ka, 2265 ka, and 2380 ka), red dots are runs with perihelion in June (Pmin: 2230 ka, 2346 ka, 2369 ka, and 2395 ka) – illustrating that eccentricity has a much larger effect on seasonality than precession at a given eccentricity.

Methods

Coccolith data acquisition

Over eight thousand samples were extracted from sediment cores for coccolithophore analysis at depth intervals to achieve a high stratigraphic resolution (0.5 to 2.3 kyr, Extended Data Table 1). Samples were prepared using the settling method[32,33]: sediments were disaggregated in water and suspensions were settled onto a 12x12 mm cover slip and mounted with Norland Optical Adhesive 74, with 8 cover slips per microscope slide. Some samples were prepared as independent duplicates. Two slides (16 samples) were placed at the same time onto the stage of an automated polarizing microscope (Leica DM6000). Following auto-focusing, 165 contiguous fields of view (with an area of 125 x 125 μm each) were imaged in each sample using a black and white SPOTFLEX camera (Diagnostic Instrument). SYRACO, a software program based on an Artificial Neural Network[34], identified all specimens belonging to 33 groups of coccolithophore taxa in the images[35]. The gephyrocapsid specimens, the dominant group studied here, were classified into six distinct classes that were merged into one group. On average, 888 Noëlaerhabdaceae coccoliths were identified in each sample. Among other morphometric parameters, size and mass of the coccoliths were measured. Coccolith mass is measured using birefringence, following published state-of-the-art methods[33,36]. The use of Artificial Intelligence in this type of work is essential because it is the only way to measure such a large number of specimens (>7 million) in a reasonable time, and thus obtain the high-resolution multi-site records required for this study.

Site-specific chronologies

IMAGES core MD97-2140[37]: The age model for Site MD97-2140[37], on the Eauripik Rise in the Western Pacific Warm Pool, is based on tuning of a high-resolution planktonic foraminiferal *Globigeronoides ruber* δ^{18}O record to the astronomically calibrated ODP Site 677 δ^{18}O *G. ruber* record[38], located in the eastern equatorial Pacific. This age model yields a chronology consistent with major micropaleontological (disappearance of *G. ruber* pink variety) and palaeomagnetic (Brunhes–Matuyama boundary) events[39].

IMAGES core MD05-2920[40] :The age model for Site MD05-2920[41], on the southern bank of Manus Island, is based on ten Accelerator Mass Spectrometer (AMS) ^{14}C dates obtained from the surface-dwelling planktonic foraminifera *G. ruber* (white), and a correlation between the benthic foraminiferal δ^{18}O record and the reference LR04 benthic foraminiferal δ^{18}O stack[18].

IMAGES core MD05-2930[40] :The age model for Site MD05-2930[42], in the Coral Sea, is based on ten AMS ^{14}C measurements of *G. ruber sensu stricto* (*ss*), and on correlation of the MD05-2930 δ^{18}O *G. ruber ss* record with the LR04 benthic foraminiferal δ^{18}O stack[18].

IODP Site U1443[43]: The age model for Site U1443, on the Ninetyeast Ridge in the southernmost Bay of Bengal, is based on correlation of physical properties data on the primary shipboard splice to the LR04 benthic foraminiferal δ^{18}O stack[18]. Physical properties were measured onboard the RV *Joides Resolution* on archive halves from all holes at Site U1443, and correlation and splicing were based on magnetic susceptibility, natural gamma ray, and reflectance spectroscopy b* data[44].

IODP Site U1448[43]: The age model for Site U1448, in the Andaman Sea, is based on correlation of the Site U1448 Ti/Ca record, derived by X-Ray Fluorescence (XRF) core scanning, to the XRF Ti/Ca record of Indian National Gas Hydrate Program (NGHP) Site 17 – a very close site with age control based on a benthic foraminiferal oxygen isotope record tuned to the LR04 benthic foraminiferal δ^{18}O stack[18,45,46].

IODP Site U1446[43]: The age model for Mahanadi Basin Site U1446 is based on correlation of a high-resolution benthic foraminiferal oxygen isotope stratigraphy to the LR04 benthic foraminiferal δ^{18}O stack[18] (S.C. Clemens, unpublished data, pers. comm.)

IODP Site U1483[47]: The age model for Scott Plateau Site U1483 is based on the shipboard integrated Magneto-biostratigraphy, and on correlation of the U1483 L* record, which presents strong G/IG variability, to the LR04 benthic foraminiferal δ^{18}O stack[18].

IODP Site U1485[47]: The age model of the northern Papua Margin Site U1485 is based on correlation between the benthic foraminiferal δ^{18}O record of this site and the LR04 benthic foraminiferal δ^{18}O stack[18].

IODP Site U1486[47]: The age model of the upper 100 m (the last 1.6 Ma) of Site U1486, from the southern bank of Manus Island, is based on a correlation between the benthic foraminiferal δ^{18}O record and the LR04 benthic foraminiferal δ^{18}O stack[18]. Below 100 m, the age model is based on the shipboard integrated magneto-biostratigraphy and correlation of the U1486 L* record (that shows strong G/IG variability) with the LR04 benthic foraminiferal δ^{18}O stack[18].

Construction of composite histograms of coccolith size and mass

The distribution of coccolith mass values is skewed toward heavy values. We therefore used the logarithm of the mass to obtain a symmetrical mass distribution. Measurements were grouped into morphological bins of 0.1 μm for coccolith length and 0.05 $\log_{10}$(pg) for coccolith mass in every sample. Samples were binned into 30-kyr time windows in each core, chosen such that it is larger than the length of a precession cycle (23-19 kyr). This will prevent any bias in the size/mass distribution resulting from changes in the relative abundance of large versus small gephyrocapsid species on precessional timescales[48]. Another advantage of using a 30 kyr time window is that the high number of measurements included in each 30 kyr bin (on average 16650 measurements) make it extremely precise but easier to discern trends. To standardise each time window at each site, the numbers contained in each bin are divided by the total number of coccoliths in that time window and multiplied by 100. To stack the records and produce evolutionary size histograms (Fig. 2a) and mass, all records are summed by bin and divided by the number of records.

Morphological Divergence Index (MDI)

In each sample, individual coccoliths were divided into two size classes: coccoliths longer and shorter than 3 μm. The average $\log_{10}$(mass) is calculated in both classes. MDI is the difference between the two averages (Extended Data Figure 2). The size of 3 μm corresponds to the best cut-off value between the two modes (2.8 and 3.9 μm) of the size distribution. Other size cut-offs were tested (2.9, 3.25 and 3.5 μm) without notable differences in the resulting MDI values and temporal trends. The records are resampled (by linear integration) at 2 kyr intervals for further analysis (time series, statistics, and stacking). A stacked record composed of all records is calculated for each time window. This stacked MDI reflects the variability seen in all individual records (Extended Data Figure 4). Because not all records cover the entire 2.8 Myr interval (3 records are over 2.3 Myr long, 3 are between 0.7 and 1.8 Myr long, and 3 are 0.4-0.6 Myr long), the stack is composed of more records in the younger part than in the older part. Because of the phase lag between MDI and eccentricity we use band-passed eccentricity (red line in Fig. 2b) to sort and bin DMI values used for Fig. 4.

Mass accumulation rates

Mass accumulation rates of Noëlaerhabdaceae coccoliths were estimated in seven cores (all cores excluding MD05-2530 and U1446) for which a quantitative sample preparation technique was applied[33]: The samples were prepared by settling onto coverslips that were weighed before and after settling, the weight difference providing the amount of sediment deposited. The number and the mass of the Noëlaerhabdaceae is estimated by SYRACO. From these quantities it is possible to estimate the weight of Noëlaerhabdaceae per gram of sediment. Noëlaerhabdaceae $CaCO_3$ MAR (only called MAR hereafter) is obtained by multiplying weight per gram by the sedimentation rate and the dry bulk density of sediment. The dry bulk density was estimated from continuous measurements of wet bulk density from gamma ray attenuation (GRAPE) and transformed by the linear relationship for each site between discrete shipboard measurements of wet bulk density and dry bulk density[49]. MARs for the 7 cores were stacked together after resampling each record at 2 kyr intervals (Fig. 3e), using the same method as for MDI. Other stacking methods, such as assembling LOESS-detrended records, were tried and produced consistent results. Differences exist between individual MAR records due to regional difference in coccolithophore productivity, export dynamics, and preservation (although only 2 cores, MD97-2140 and U1443, were retrieved from sediments deeper than 2000 m). However, three common patterns emerge in all individual records: an increasing trend in MAR towards the present, a sharp stepwise increase at ~1 Ma, and the clear presence of eccentricity cycles. Noëlaerhabdaceae coccolith flux (Extended Data Figure 5c) is calculated as the number of coccoliths per gram of sediment multiplied by the sedimentation rate.

Time series analysis

Time series analyses were performed using the software packages Analyseries[50] and Acycle[51] on detrended records. Cross-spectral analyses were performed in Analyseries using Blackman-Turkey transforms[52]. For evolutive analyses (Fig. 3) a window of 500 kyr (250 data points) and a step of 100 kyr was used. Coherence values above 0.56 are above the 80% confidence level (Fig. 2b). Spectral analyses were performed with the Multi Taper Method (MTM)[53] with both evolutive and entire series (Extended Data Figure 1). Spectral properties are similar in all individual MDI records, and show that the absence of precession (19-23 kyr) and obliquity (~41 kyr) is not a result of chronological bias in constructing the stack that would have smoothed the record. Each record has a ~2 kyr resolution with a precise independent age model. The absence of precession and obliquity is therefore a common and robust feature of all of the MDI series as well as the stacked record.

Low-pass filters

We designed 2nd order low-pass filters in order to reproduce the effect of the time needed for a new evolved species to fully succeed (200 kyr for *E. huxleyi*). We transformed the following classical low-pass filter complex transfer function *H*:

$$H(j\omega) = \frac{A}{1+\frac{j\ \omega}{Q\omega_0}-\frac{\omega}{\omega_0}^2}$$

(where A is the amplitude, Q is the quality factor, ω is the angular frequency $2\pi f$, (f the frequency)) in its associated differential equation:

$\frac{d^2y}{dt^2} + \frac{\omega_0}{Q}\frac{dy}{dt} + \omega_0^2 y = \omega_0^2 x$ where y is the output series and x the input series.

We solved it numerically as follow:

$$y_t = \frac{1}{1+\frac{\omega_0}{Q}+\omega_0^2}((2+\omega_0)y_{t-1} - y_{t-2})A\omega_0^2 x_t$$

Two configurations have been chosen: one produces a delay of 200 kyr for the new species' success, the second produces a delay of 130 kyr (Extended Data Figure 8a). To obtain those delays, we used the following values:

First case (delay of 200 kyr), ω_0 = 0.021, Q = 1, A = 1

Second case (delay of 130 kyr), ω_0 = 0.035, Q = 1.02, A = 0.65

The delay of 200 kyr corresponds to the time between the First Appearance Datum (FAD) and the beginning of the acme (BA) of *E. huxleyi*[17]. The FAD of this species is well documented because its characteristic T shape elements are a morphological feature that appeared suddenly, without gradation. The other *Gephyrocapsa* species have been described using criteria that are subject to gradation between species: coccolith length, size of the central opening, and orientation of the bridge[54]. For example, the FAD of a typical *G. ercisonii*, (a small gephyrocapsid) that appeared at about the same time as *E. huxleyi*[3] is not reported precisely because it evolved progressively from *G. caribbeanica* (a mid-size species). It is interesting to note that the FAD and the BA of *E. huxleyi* occurred similarly in times of eccentricity decrease, but two cycles apart. The intermediate cycle may have been too high to allow *E. huxleyi* to begin its dominance. This may not have been the case for other species under different orbital configurations. This is why we did a filter with a different configuration, which produces a delay of about one eccentricity cycle between a FAD and a BA. In order to express the response of those filters, we built their Bode magnitude plots, expressing the frequency response, and their Bode phase plots, expressing the phase shift (Extended Data Figure 8b, c).

Model Description

To simulate changes in Net Primary Production (NPP) related to changes in eccentricity we used the Earth System Model IPSL-CM5A2[5] that simulates the interactions between ocean, atmosphere, land and ice. The following section provides a brief description of model components and experiments setup. We then describe the model behaviour at low eccentricity and discuss how the large-scale ocean-atmosphere circulation at high eccentricity in our simulations compare to previous modelling studies.

The IPSL-CM5A2 coupled model is a combination of the LMDz5A atmospheric model[55], the ORCHIDEE[56] land surface model and the NEMOv3.6 oceanic model[57]. The NEMO model includes an ocean dynamic component (OPA[58]), a sea-ice thermodynamics model (LIM2[59]) as well as a biogeochemistry model (PISCES-v2[6]) and has an horizontal resolution of 2° by 2° (refined to 0.5° in the tropics) and 31 vertical levels, whose thickness increases from 10 m at the surface to 500 m at the bottom. The atmospheric grid has a horizontal resolution of 1.875° in latitude by 3.75° in longitude with 39 vertical levels. The ocean-atmosphere coupling is ensured by the OASIS coupler[60] that interpolates and exchange variables between the two components. Detailed description of IPSL-CM5A2 and performances in simulating pre-industrial climate can be found in references 61,62. PISCES-v2 simulates the main oceanic biogeochemical cycles (C, P, Si, N and Fe) and has a simple representation of the lower trophic levels of the marine ecosystem[6], with two phytoplankton (nannophytoplankton and diatoms) and two zooplankton (micro- and meso-zooplankton) size classes and five limiting nutrients (Fe, NO_3^-, NH_4^+, Si and PO_4^{3-}). Phytoplankton growth is controlled by nutrients, light availability, and water temperature. In the version of the model we used, river supply to the ocean of all elements apart from DIC and alkalinity is taken from the GLOBAL-NEWS2 data sets[63] and does not vary from one simulation to another. Model parameterizations are detailed in reference 6.

Simulations were performed for seven early Pleistocene time slices and differ only by their respective orbital parameters (Extended Data Table 2, Figure 2). The time slices were chosen in order to target the signal produced by the 405-kyr eccentricity cycle. Land-sea mask, ice-sheets configuration as well as CO_2 and other greenhouse gases concentrations are set at pre-industrial values. Each simulation was started from the same equilibrated pre-industrial simulation[62] and was run for 500 years. NPP is integrated over the whole water-column and averaged over the last 100 model years.

At low eccentricity (EminPmax and EminPmin) the eastern Indian ocean surface dynamics is forced by the summer westerlies that blow northward over the Bay of Bengal (Extended Data Figure 6f), associated with high precipitation over India and the Himalayan foreland region, while strong easterlies are recorded south of the equator. Winds force strong westward surface currents along the equator and south of Sumatra Island that generate upwelling (Extended Data Figure 7b). The latter advects nutrients to the surface (Extended Data Figure 7a) and triggers high productivity during summer. This peak productivity contributes to the strong seasonal cycle in this region. The winds reverse during boreal winter, triggering a second productivity bloom of lesser intensity (not shown). The productivity minimum is recorded during late spring when low-level winds along the equator are weak westerlies that favour downwelling and prevent strong convective mixing, which results in lower nutrient content within the surface layer of the ocean. The seasonal cycle of productivity in this region is very similar to the cycle simulated for the present-day EIO[64].

At high eccentricity, the simulated patterns of atmosphere-ocean circulation and surface ocean physical state (Extended Data Figure 6g-j and 8b, c) are in line with previous modelling study under similar orbital configurations[65-67]. In addition, our simulations also illustrate how these changes impact the seasonal productivity cycle. The increasing amplitude of the seasonal cycle in the surface ocean at high eccentricity is probably not limited to the IPWP area. For example, Erb *et al.*[68] also simulate enhancement of the surface ocean temperature cycle at high eccentricity in the Eastern Equatorial Pacific, with higher amplitude that in the Western Equatorial Pacific.

Methods references

32 Beaufort, L. Adaptation of the random settling method for quantitative studies of calcareous nannofossils. *Micropaleontology* **37**, 415-418 (1991).

33 Beaufort, L., Barbarin, N. & Gally, Y. Optical measurements to determine the thickness of calcite crystals and the mass of thin carbonate particles such as coccoliths. *Nat. Protoc.* **9**, 633-642, doi:10.1038/nprot.2014.028 (2014).

34 Beaufort, L. & Dollfus, D. Automatic recognition of coccolith by dynamical neural network. *Mar. Micropaleontol.* **51**, 57-73, doi : 10.1016/j.marmicro.2003.09.003 (2004).

35 Barbarin, N. *La reconnaissance automatisée des nannofossiles calcaires du Cénozoique.* Doctorat thesis, Aix-Marseille Université, (2014).

36 Beaufort, L. Weight estimates of coccoliths using the optical properties (birefringence) of calcite. *Micropaleontology* **51**, 289-298, doi: 10.2113/gsmicropal.51.4.289 (2005).

37 de Garidel-Thoron, T., Rosenthal, Y., Bassinot, F. C. & Beaufort, L. Stable sea surface temperatures in the western Pacific warm pool over the past 1.75 million years. *Nature* **433**, 294-298, doi: 10.1038/nature03189 (2005).

38 Shackleton, N. J. *et al.* An alternative astronomical calibration of the lower Pleistocene timescale based on ODP Site 677. *T. Rse. Earth* **81**, 251-261, doi: 10.1017/S0263593300020782 (1990).

39 Carcaillet, J. T., Thouveny, N. & Bourlès, D. L. Geomagnetic moment instability between 0.6 and 1.3 Ma from cosmonuclide evidence. *Geophys. Res. L.* **30**, 1792, doi: 10.1029/2003GL017550 (2003).

40 Beaufort, L. & Shipboard Scientific Party. *MD148/PECTEN.* (Institut Polaire Francais, 2005).

41 Tachikawa, K. *et al.* The precession phase of hydrological variability in the Western Pacific Warm Pool during the past 400 ka. *Quaternary Sci. Rev.* **30**, 3716-3727, doi: 10.1016/j.quascirev.2011.09.016 (2011).

42 Regoli, F. *et al.* Progressive shoaling of the equatorial Pacific thermocline over the last eight glacial periods. *Paleoceanography* **30**, 439-455, doi: 10.1002/2014PA002696 (2015).

43 Clemens, S. C., Kuhnt, W., LeVay, L. J. & the Expedition 353 Scientists Indian monsoon rainfall. *IODP Preliminary Report* **353**, doi: 10.14379/iodp.pr.353.2015 (2015).

44 Clemens, S. C. Site U1443. - *Proceedings of the International Ocean Discovery Program; Indian monsoon rainfall; Expedition 353 of the riserless drilling platform from and to Singapore; Sites U1443-U1443, 29 November 2014-29 January 2015* **353**, 41-41 (2016).

45 Gebregiorgis, D. *et al.* Southern Hemisphere forcing of South Asian monsoon precipitation over the past ~1 million years. *Nat. Commun.* **9**, 4702, doi: 10.1038/s41467-018-07076-2 (2018).

46 Gebregiorgis, D. *et al.* What can we learn from X-ray fluorescence core scanning data? A paleomonsoon case study. *Geochem. Geophy. Geosy.* **21**, e2019GC008414, doi: 10.1029/2019GC008414 (2020).

47 Rosenthal, Y., Holbourn, A. E., Kulhanek, D. K. & the Expedition 363 Scientistsin *IODP proceeding* Vol. 363 (ed IODP) 69 (Texas A&M University, College Station TX, USA, 2017).

48 Beaufort, L., Bassinot, F. C. & Vincent, E. in *Reconstructing Ocean History: a window into the future* (eds F. Abrantes & A.C. Mix) 245-272 (Kluwer Academic/Plenum Publisher, 1999).

49 Lyle, M. Vol. 18 (2003).

50 Paillard, D., Labeyrie, L. & Yiou, P. Macintosh program performs time-series analysis. *Eos Trans. AGU,* **77**, 379, doi: 10.1029/96EO00259 (1996).

51 Li, M., Hinnov, L. & Kump, L. Acycle: Time-series analysis software for paleoclimate research and education. *Comput. Geosci.* **127**, 12-22, doi: 10.1016/j.cageo.2019.02.011 (2019).

52 Blackman, R. B. & Tukey, J. W. The measurement of power spectra from the point of view of communications engineering—Part I. *Bell Syst. Tech. J.* **37**, 185-282, doi: 10.1002/j.1538-7305.1958.tb03874.x (1958).

53 Thomson, D. J. Spectrum estimation and harmonic analysis. *Proc. IEEE* **70**, 1055-1096, doi: 10.1109/PROC.1982.12433 (1982).

54 Bollmann, J. Morphology and biogeography of the *Gephyrocapsa* coccoliths in Holocene sediments. *Mar. Micropaleontol.* **29**, 319-350, 10.1016/S0377-8398(96)00028-X (1997).

55 Hourdin, F. *et al.* Impact of the LMDZ atmospheric grid configuration on the climate and sensitivity of the IPSL-CM5A coupled model. *Clim. Dyn.* **40**, 2167-2192, doi: 10.1007/s00382-012-1411-3 (2013).

56 Krinner, G., Ciais, P., Viovy, N. & Friedlingstein, P. A simple parameterization of nitrogen limitation on primary productivity for global vegetation models. *Biogeosciences Discuss.* **2**, 1243-1282, doi : 10.5194/bgd-2-1243-2005 (2005).

57 Madec, G. & Nemo, T. NEMO ocean engine. *Note du Pôle de modélisation de l'Institut Pierre□Simon Laplace* **27** (2015).

58 Madec, G. NEMO reference manual, ocean dynamics component: NEMO-OPA. *Preliminary version. Note du Pole de modélisation, Institut Pierre-Simon Laplace (IPSL), France*, 1288-1161 (2008).

59 Fichefet, T. & Maqueda, M. M. Sensitivity of a global sea ice model to the treatment of ice thermodynamics and dynamics. *J. Geophys. Res. Oceans* **102**, 12609-12646, doi: 10.1029/97JC00480 (1997).

60 Valcke, S. *et al.* Coupling technologies for earth system modelling. *Geosci. Model Dev.* **5**, 1589-1596, doi: 10.5194/gmd-5-1589-2012 (2012).

61 Dufresne, J.-L. *et al.* Climate change projections using the IPSL-CM5 Earth System Model: from CMIP3 to CMIP5. *Clim. Dyn.* **40**, 2123-2165, doi: 10.1007/s00382-012-1636-1 (2013).

62 Sepulchre, P. *et al.* An Earth System Model designed for long simulation of past and future climates. *Geosci. Model Dev.* **13**, 3011-3053, doi: 10.5194/gmd-13-3011-2020 (in review).

63 Mayorga, E. *et al.* Global nutrient export from WaterSheds 2 (NEWS 2): model development and implementation. *Environ. Model. Softw.* **25**, 837-853, doi: 10.1016/j.envsoft.2010.01.007 (2010).

64 Koné, V., Aumont, O., Lévy, M. & Resplandy, L. Physical and biogeochemical controls of the phytoplankton seasonal cycle in the Indian Ocean: A modeling study. In *Indian Ocean Biogeochemical Processes and Ecological Variability* (eds J.D. Wiggert, R.R. Hood, S.A. Naqvi, K.H. Brink and S.L. Smith) **185**, 350, doi: 10.1029/2008GM000700 (2009).

65 Bosmans, J. *et al.* Response of the Asian summer monsoons to idealized precession and obliquity forcing in a set of GCMs. *Quaternary Sci. Rev.* **188**, 121-135, doi: 10.1016/j.quascirev.2018.03.025 (2018).

66 Braconnot, P. & Marti, O. Impact of precession on monsoon characteristics from coupled ocean atmosphere experiments: changes in Indian monsoon and Indian ocean climatology. *Mar. Geol.* **201**, 23-34, doi: 10.1016/S0025-3227(03)00206-8 (2003).

67 Prescott, C., Haywood, A., Dolan, A., Hunter, S. & Tindall, J. Indian monsoon variability in response to orbital forcing during the late Pliocene. *Global Planet. Change* **173**, 33-46, doi: 10.1016/j.gloplacha.2018.12.002 (2019).

68 Erb, M. P. *et al.* Response of the equatorial pacific seasonal cycle to orbital forcing. *J. Climate* **28**, 9258-9276, doi: 10.1175/JCLI-D-15-0242.1 (2015).

69 Chen, M.-T. & Beaufort, L. Exploring quaternary variability of the east Asia monsoon, Kuroshio Current, and western Pacific warm pool systems: High-resolution investigations of paleoceanography from the IMAGES III (MD106) IPHIS cruise. *TERRESTRIAL ATMOSPHERIC AND OCEANIC SCIENCES* **9**, 129-142 (1998).

70 Gartner, S. Paleoceanography of the mid-Pleistocene. *Mar. Micropaleontol.* **13**, 23-46, doi: 10.1016/0377-8398(88)90011-4 (1988).

71 Pujos, A. & Giraudeau, J. Distribution of Noelaerhabdaceae (calcareous nannofossils) in the upper and middle Quaternary of the Atlantic and Pacific oceans. *Oceanol. Acta* **16**, 349-362 (1993).

Acknowledgments

This paper is a contribution of the Climate research group at CEREGE. This research uses samples provided by the IODP, which is sponsored by the U.S. National Science Foundation and participating countries under management of Joint Oceanographic Institutions, Inc. We thank the shipboard participants of IODP Expeditions 353 and 363 and IMAGES Expeditions 3 and 13. The authors acknowledge French ANR projects CALHIS (LB), iMonsoon (CTB), AMOR (YD), and INSU project CALVE (CTB) which provided funding for this work. IODP-France provided post-cruise funding to LB and CTB. A. Fruy and S. Sergi are thanked for sample preparation assistance. We thank the CEA/CCRT for providing access to the HPC resources of TGCC under the allocation 2019-A0070102212 made by GENCI.

Author Contributions

LB designed the study. LB, YG, NB and MT developed automated artificial intelligence methods. LB, CTB, JCM, PC, EG, and SB prepared samples and/or generated data. ACS designed and ran the model simulations, in collaboration with YD. LB and CTB analysed the morphometric data. LB, CTB, ACS, BSM, YD, and YR discussed interpretations. LB, CTB and ACS wrote the manuscript with important contributions from BSM, YD, and YR.

Additional Information

Correspondence and requests for materials should be addressed to Luc Beaufort (beaufort@cerege.fr). Reprints and permissions information is available at www.nature.com/reprints.

Competing interest declaration

The authors declare no competing interests.

Extended Data Figures and Tables

Site	Expedition	Longitude	Latitude	Water Depth (m)	Biome	Record length (kyr)	Mean Resolution (kyr)	Number of samples	Number of Measurements
U1446	IODP 353	85°441	19°050 N	1440	INDE	468	0.5	952	222 119
U1448	IODP 353	93°00.00	10°38.03 N	1096	MONS	716	1.1	624	617 138
U1443	IODP 353	90°21.71	5°23.01 N	2940	MONS	2818	1.6	1717	1 337 793
MD97-2140	IMAGES 3	141°45.49	2°02.59 N	2547	WARM	1758	1.4	1241	540 523
U1486	IODP 363	144°36.08	2°22.34 S	1332	WARM	2661	2.2	1195	1 004 860
MD05-2920	IMAGES 13	144°32	2°51.48 S	1843	WARM	387	1.1	353	436 984
U1485	IODP 363	142°47.59	3°06.16 S	1145	SUND	535	0.9	587	580 612
MD05-2930	IMAGES 13	146°15.73	10°25.30 S	1490	AUSE	793	2.1	372	620 736
U1483	IODP 363	121°5.24	13°05.24 S	1733	ISSG	2332	2.3	994	1 777 406
							Average = 1.6	Sum =8035	Sum=7 138 171

Extended Data Table 1: Characteristics of the nine marine records used in this study. Biome codes[20]: INDE = Eastern India Coastal province, MONS = Indian Monsoon Gyres Province, WARM = Western Pacific Warm Pool province, SUND = Sunda-Arafura Shelves Province, AUSE = East Australian Coastal Province, ISSG = Indian South Subtropical Gyre Province. These cores were retrieved during four expeditions: IMAGES 3[69] and 13[40], and International Ocean Discovery Program (IODP) Expeditions 353[43] and 363[47], which took place in the Western Pacific and Indian Tropical Oceans (Figure 1).

Configuration (kyr)	Eccentricity	Precession	Longitude of perihelion (°)	Obliquity (°)	Mean YCR at Equator ($W.m^{-2}$)
C2222 (EmaxPmax)	0.054	0.054	87	23.73	74
C2230 (EmaxPmin)	0.053	-0.037	315	23.84	83
C2265	0.026	0.024	115	24.28	59
C2346	0.034	-0.033	287	24.27	62
C2369	0.016	-0.015	256	22.26	52
C2380 (EminPmax)	0.006	0.006	77	23.74	37
C2395 (EminPmin)	0.005	-0.003	310	23.42	39

Extended Data Table 2: Summary of orbital parameters[19] used for each simulation and Mean Yearly Contrast of Radiation at Equator (Wm^{-2}) derived from IPSL-CM5A2 (see Methods).

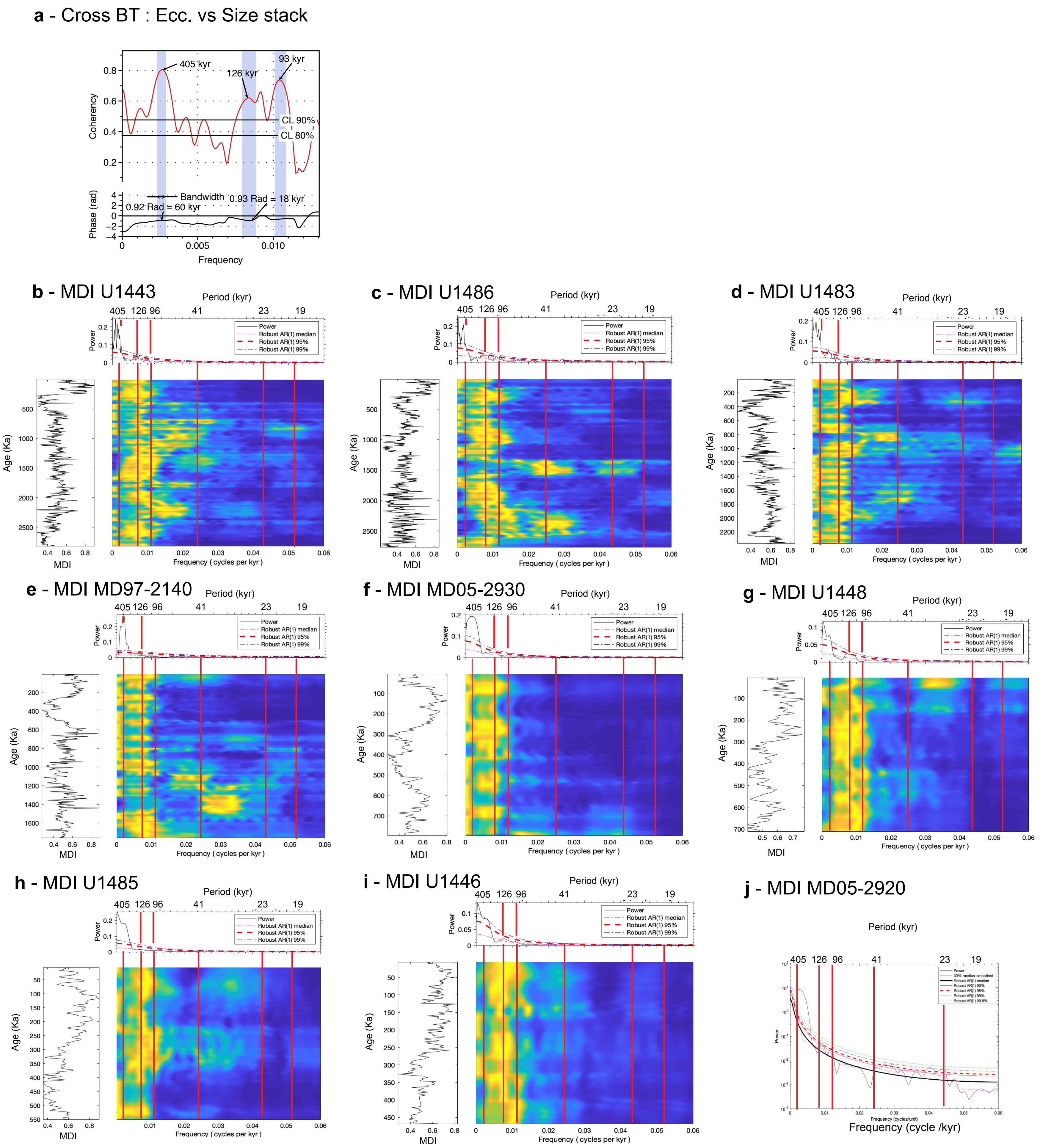

Extended Data Figure 1: **a**: Cross-spectral analysis between eccentricity and stacked average coccolith length. Top: coherency; Bottom: phase (radian). **b to j**: MTM and evolutive spectral analyses (see Methods) of detrended individual MDI series resampled at 2 kyr intervals (shown on left of each evolutive analysis. Primary orbital periods are shown by red lines.

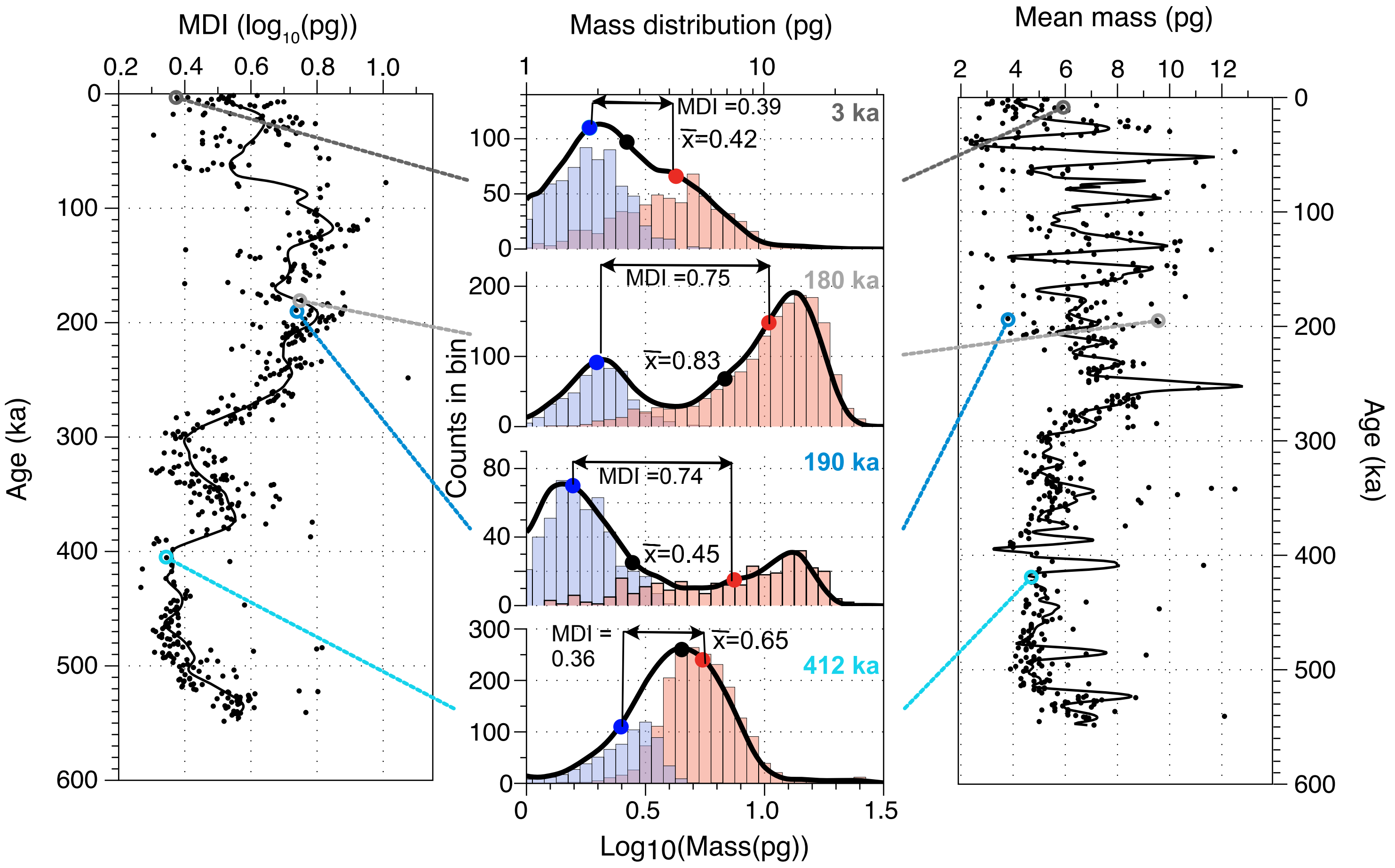

Extended Data Figure 2: Schematic illustrating how MDI is calculated (also see Methods), and how it represents morphological diversity, using data from Site U1485 as an example. In each sample, two size classes are created: coccoliths shorter and longer than 3 μm (blue and red histograms). The average log(mass) is calculated in both classes (blue and red dots on the histograms). MDI is the difference between these two averages. Thus, MDI can differ substantially from average coccolith mass of the whole population (black dots on mass distribution plots), and two samples can have a similar MDI but very different average mass and mass distributions (e.g., examples at 180 ka and 190 ka), or very different MDI but similar averages (e.g., 3 ka vs 190 ka). In this way, MDI isolates morphology variability that results from evolutionary contractions and dilations in the number of different morphotypes present within the population.

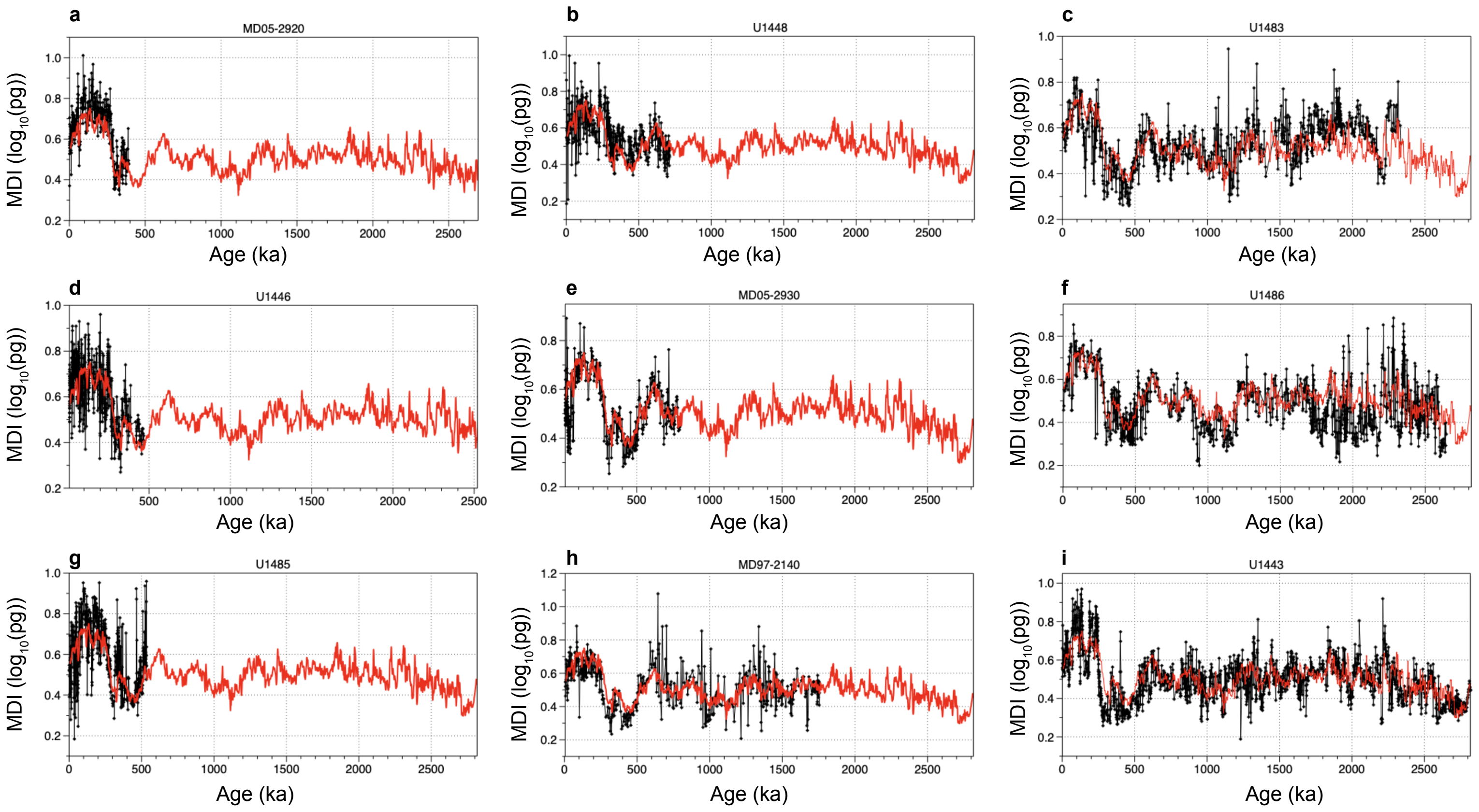

Extended Data Figure 3: Individual MDI records for each site (black lines and points) plotted with the stacked MDI record (red line). Pearson correlation coefficients between individual sites and the stack vary between 0.71 and 0.93 (p-values are all <0.00001).

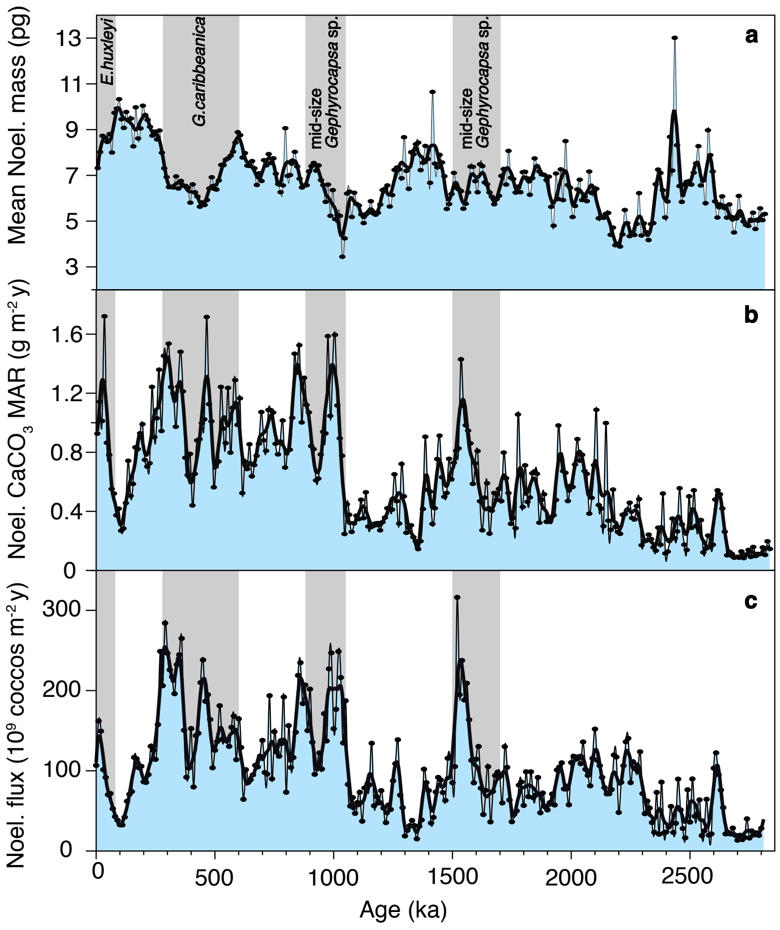

Extended Data Figure 4: Figure comparing stacked records, binned into 10-kyr intervals, of Noëlaerhabdaceae average coccolith mass (**a**), Noëlaerhabdaceae $CaCO_3$ mass accumulation rates (**b**), and Noëlaerhabdaceae coccolith flux to the seafloor (**c**) (see Methods). Grey shaded areas represent four described acmes of mid-size Noëlaerhabdaceae species[15-17,70,71].

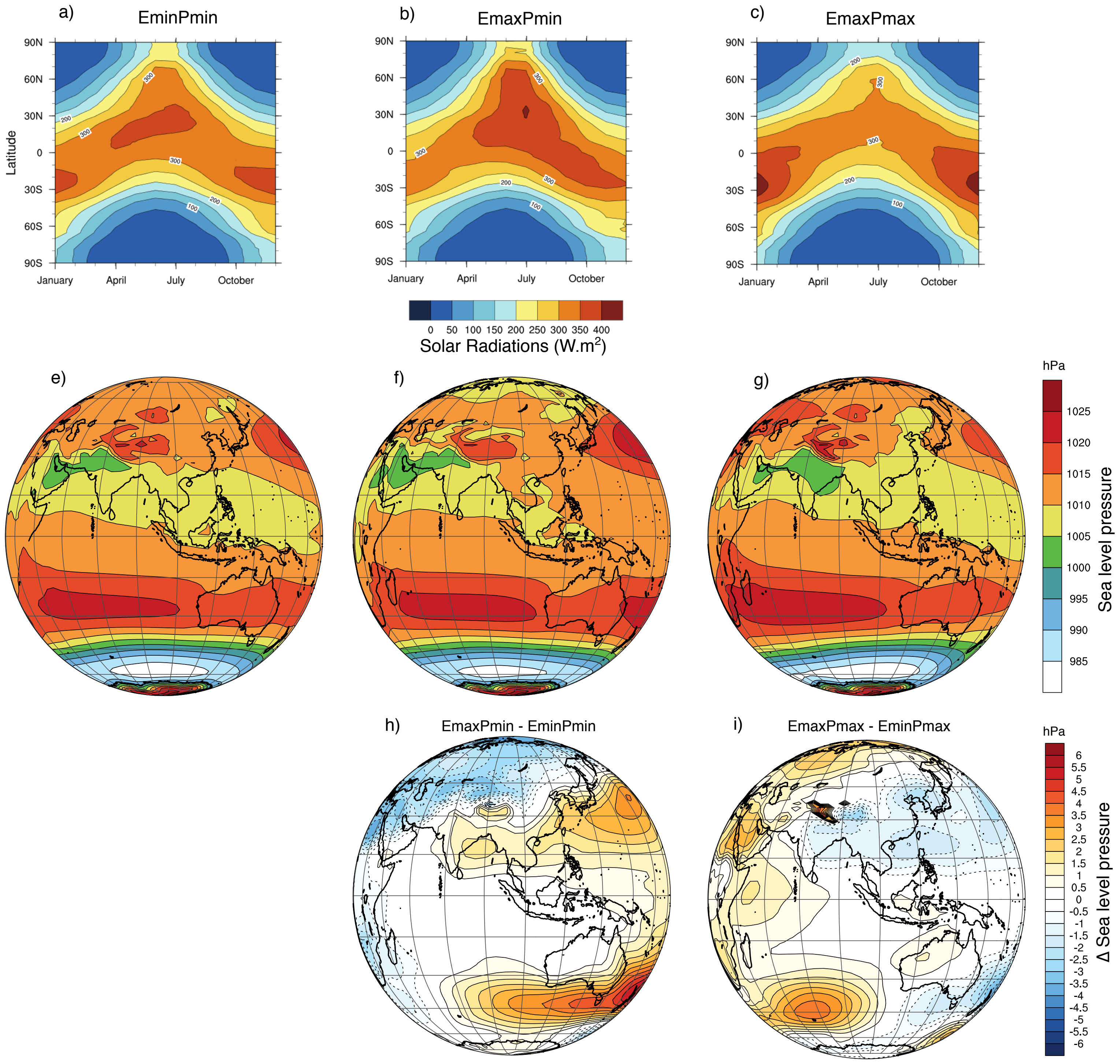

Extended Data Figure 5: Top: Yearly maximum contrast in NPP (gC.m^{-2}.day^{-1}) for (a) EminPmin, (b) EmaxPmin and (c) EmaxPmax. Low eccentricity values minimise the amplitude of precession variability (Extended Data Figure 7a-c), thus we only show results for minimum precession value at minimum eccentricity (EminPmin) but the reader can consider those results to be similar for the EminPmax simulation. (d) and (e) represent the anomaly of yearly maximum contrast in NPP. At EmaxPmax, the eastern equatorial Indian Ocean exhibits moderate seasonality (a) due to inhibition of the summer productivity induced by lower nutrient concentrations in this area (Extended Data Figure 8a). In this case, high productivity areas during boreal summer are shifted to south-west of India. Bottom: Late summer (JASO) low-level winds for (f) EminPmin (g) EmaxPmin (h) EmaxPmax simulations. (i) and (j) represent the anomaly in late summer low-level winds. At EmaxPmax the north-equatorial westerlies (c, e) are confined to south of 10°N due to the extension above India of the low-pressure area (Figure 1).

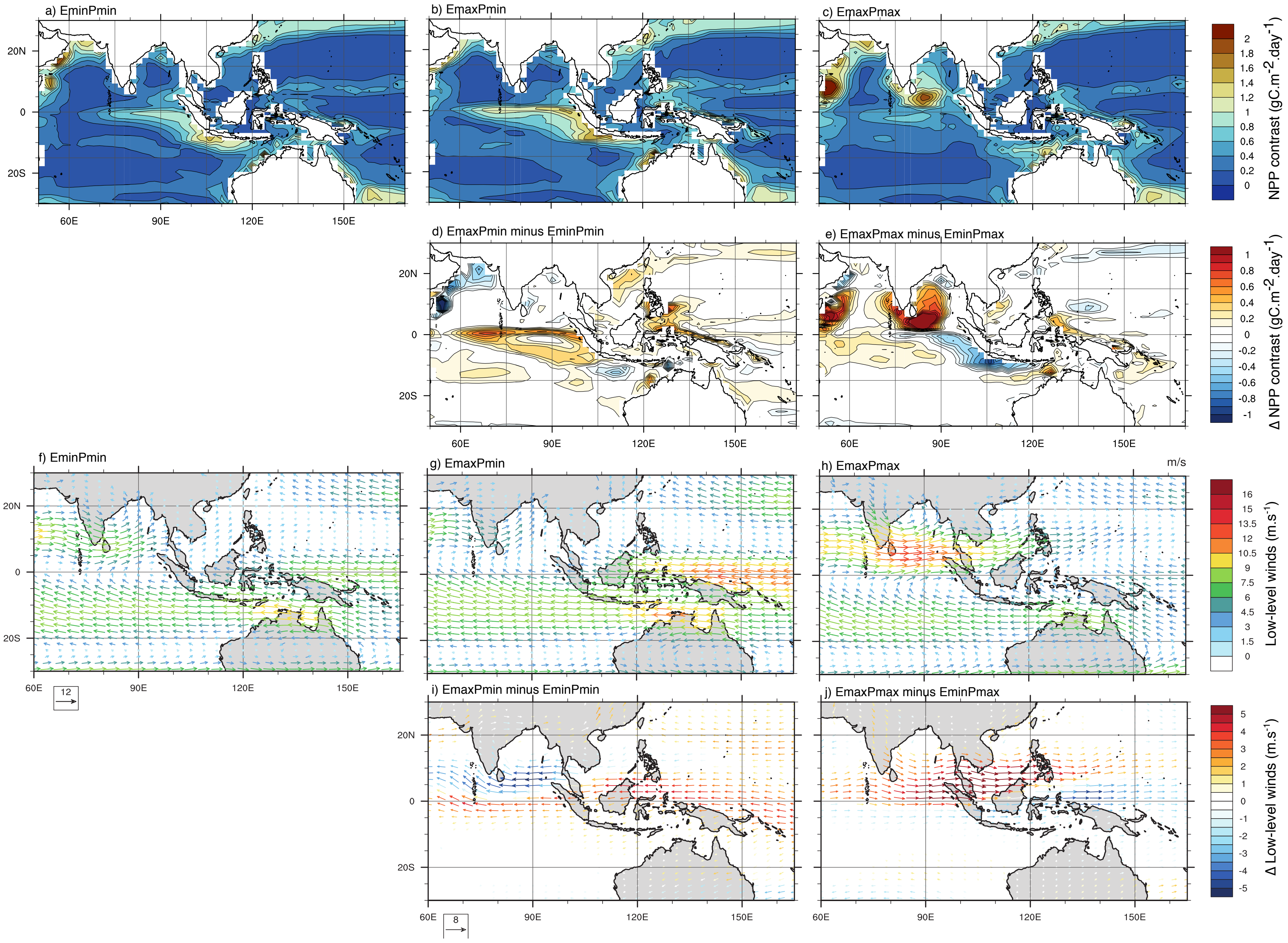

Extended Data Figure 6: Seasonal latitudinal variations of solar radiation at the top of the atmosphere derived from the model (W.m^{-2}). (a) EminPmin, (b) EmaxPmin, (c) EmaxPmax. See Extended Data Table 2 for details of orbital configurations of each simulation. Late summer (JASO) low-level winds for (d) EminPmin (e) EmaxPmin (f) EmaxPmax simulations and anomaly in late summer low-level winds (g) EmaxPmin minus EminPmin (h) EmaxPmax minus EminPmax.

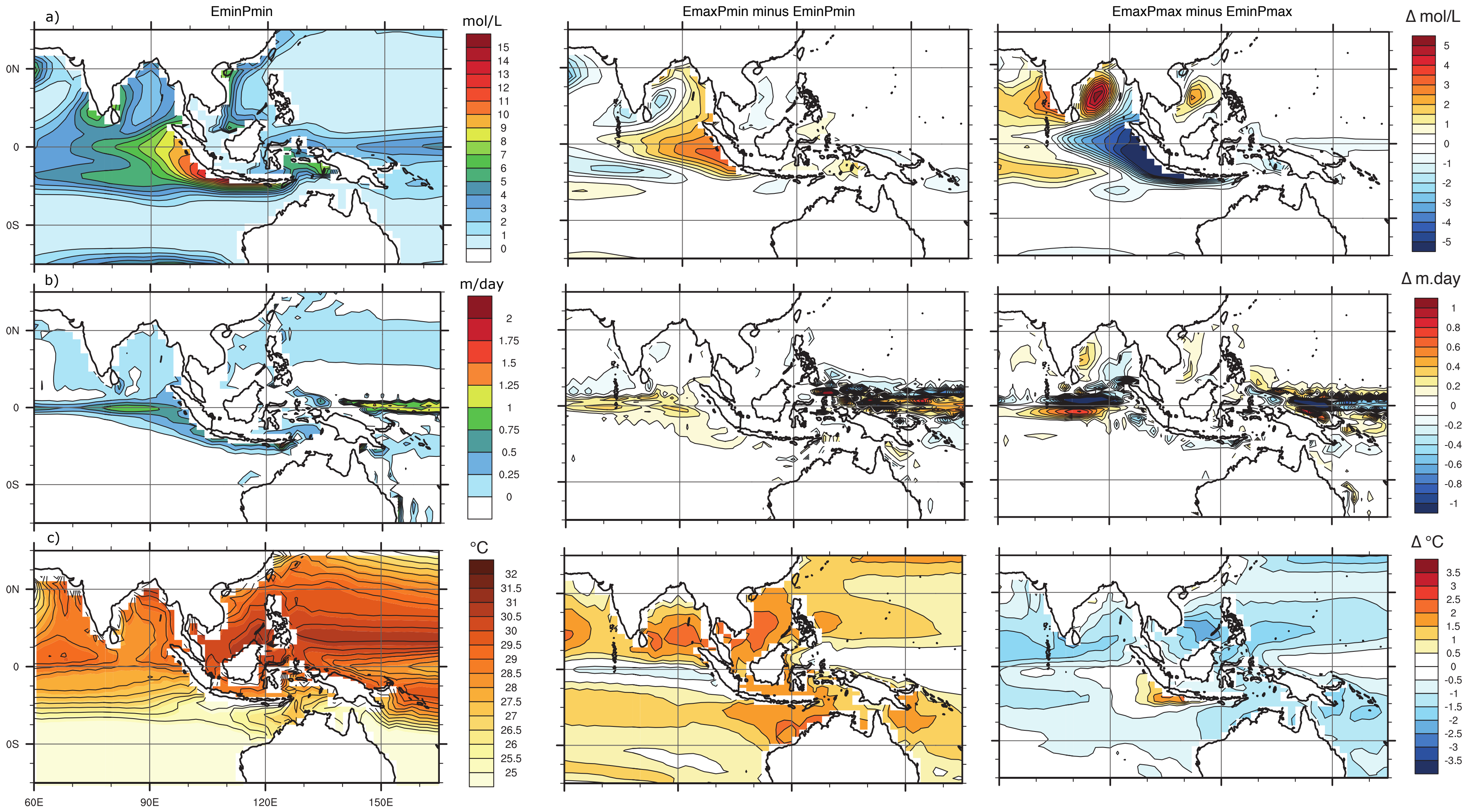

Extended Data Figure 7: (a) NO_3 concentrations in the surface layer (0-100m), (b) upwelling velocity (averaged between 40 and 80m), (c) SST. All variables are averaged over JASO. Left : Emin, Middle : EmaxPmin minus EminPmin, Right : EmaxPmax minus EminPmax.

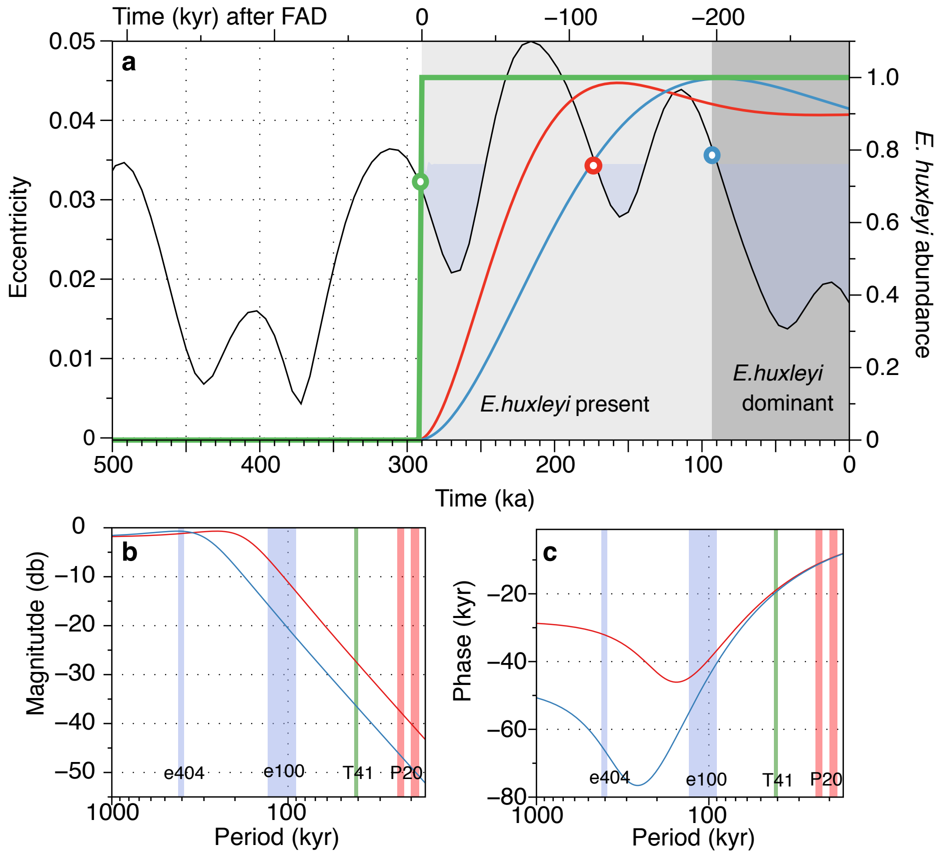

Extended Data Figure 8: **a** and **b**: Bode plots of the 130 kyr delay filter (red) and the 200 kyr delay filter (blue) for magnitude (a) and phase (b) (see Methods). Earth's primary orbital periods are indicated by shading. **c**: Low-pass filter design, for the delay between First Appearance Datum (FAD) and the beginning of the acme (BA) for *E. huxleyi* (blue line) and other gephyrocapsids (red line). The stepped green line represents *E. huxleyi*'s existence (filtered such that 0 means absence and 1 presence). The blue and red curves are the output series of the 2 low-pass filters described in the methods. The black curve represents coeval eccentricity values.

Data and Code availability

All morphological data are available at www.microautomate.cerege.fr/data/evolseason.

LMDZ, XIOS, NEMO and ORCHIDEE are released under the terms of the CeCILL license. OASIS-MCT is released under the terms of the Lesser GNU General Public License (LGPL). IPSL-CM5A2 source code is publicly available through svn, with the following commands line:

```
svn co http://forge.ipsl.jussieu.fr/igcmg/svn/modipsl/branches/publications/IPSLCM5A2.1_11192019 modipsl ; cd modipsl/util ; ./model IPSLCM5A2.1
```

The mod.def file provides information regarding the different revisions used, namely:

- NEMOGCM branch nemo_v3_6_STABLE revision 6665
- XIOS2 branchs/xios-2.5 revision 1763
- IOIPSL/src svn tags/v2_2_2
- LMDZ5 branches/IPSLCM5A2.1 rev 3591
- branches/publications/ORCHIDEE_IPSLCM5A2.1.r5307 rev 6336
- OASIS3-MCT 2.0_branch (rev 4775 IPSL server)

The login/password combination requested at first use to download the ORCHIDEE component is anonymous/anonymous. We recommend that you refer to the project website: http://forge.ipsl.jussieu.fr/igcmg_doc/wiki/Doc/Config/IPSLCM5A2 for a proper installation and compilation of the environment.